Full elastic strain tensor determination at the phase scale in a powder metallurgy nickel-based superalloy using X-ray Laue microdiffraction

Gader Altinkurt,[a,b] Mathieu Fèvre,[a]* Odile Robach,[c,d] Jean-Sébastien Micha,[c,d,e] Guillaume Geandier[b] and Moukrane Dehmas[f]

[a]Laboratoire d'Étude des Microstructures, UMR 104 CNRS-ONERA, 92322 Châtillon, France, [b]IJL, UMR 7198 CNRS-Université de Lorraine, Nancy, France, [c]Université Grenoble Alpes, 38000 Grenoble, France, [d]CEA-INAC-MEM, 17 rue des Martyrs, 38000 Grenoble, France, [e]CNRS, 17 rue des Martyrs, 38000 Grenoble, France, and [f]CIRIMAT, UMR 5085 CNRS-UPS-INPT-ENSIACET, 31000 Toulouse, France. *Correspondence e-mail: mathieu.fevre@onera.fr

Keywords: Laue microdiffraction; full strain tensor; nickel-based superalloys; phase sensitivity.

Laue microdiffraction is used to determine the full elastic strain tensor of the γ and γ' phases in grains of a nickel-based superalloy with a coarse-grained microstructure. A 'rainbow' filter and an energy dispersive point detector are employed to measure the energy of Bragg reflections. For the two techniques, an uncertainty of $\pm 2.5 \times 10^{-3}$ Å is obtained for the undetermined crystal lattice parameter. Our measurements show that the filter method provides better confidence, energy resolution, accuracy and acquisition time. The sensitivity of each method with respect to the γ–γ' lattice mismatch is demonstrated with measurements in samples with average precipitate sizes of 200 and 2000 nm. For the 200 nm precipitate size, the lattice mismatch is less than 2×10^{-3} Å and the dilatational strains are close to $\pm 1.5 \times 10^{-3}$ depending on the considered phase. For the 2000 nm precipitate size, the lattice mismatch is close to 8×10^{-3} Å and almost no elastic strain occurs in the microstructure.

1. Introduction

Residual stresses play an important role in the fatigue of aero-engine critical parts and are extensively studied both experimentally and numerically for safety, performance and cost reduction purposes. In nickel-based powder metallurgy superalloys, the chemical composition, the grain size, the precipitate microstructure, and the lattice mismatch between the γ and γ' phases are used as parameters to design alloys with specific mechanical properties. Residual elastic stresses generated by the manufacturing process and their relaxation caused by thermal and mechanical loadings are most often investigated at the macroscopic scale with the $\sin^2\psi$ method for fine-grained microstructures (Cao *et al.*, 1994; Dye *et al.*, 2004; Buchanan & John, 2014) and with the Ortner method for single crystals (Morançais *et al.*, 2015). Generally, results correspond to the average alloy and few papers report on the phase sensitivity of internal stresses (Stone, Reed & Holden, 1999; Stone, Holden & Reed, 1999; Connor *et al.*, 2014; Preuss *et al.*, 2008). For the investigation of coarse-grained microstructures (40 < grain size < 400 µm), the $\sin^2\psi$ method can still be employed by using high-energy X-rays or neutrons when a sufficient number of grains diffract. Then, measured quantities correspond to averages in mm^3 or cm^3 gauge volumes. In such microstructures, measurement at the grain scale would provide a better understanding of the relationship between the residual stresses, the alloy features and its mechanical properties. It would also improve the development of models (*e.g.* crystal plasticity based methods).

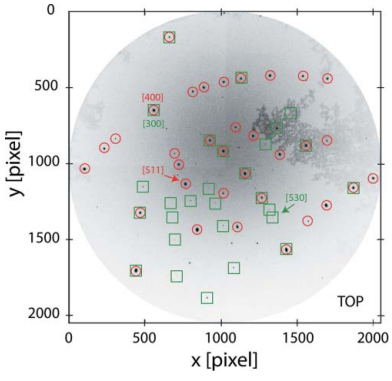

In nickel-based superalloys, γ' precipitates exhibit a cube–cube orientation relationship with the γ matrix. Owing to the small lattice mismatch between the two phases ($\Delta a \simeq 10^{-3}$ Å), high-resolution diffractometers and peak profile analyses are required to separate the contribution of each phase in a diffraction experiment. This technique has been applied in laboratories and large instrument facilities to measure lattice mismatches in cuboidal or rafted microstructures and diffraction elastic constants [see for example Hazotte *et al.* (1992), Royer *et al.* (1997), Stone, Holden & Reed (1999), Aba-Perea *et al.* (2016) and references therein]. Accurate determination of γ and γ' strains using diffraction techniques is challenging because several tens of diffraction peaks must be recorded and the energy bandwidth must be small enough that peak profiling can be performed. To our knowledge, full strain tensor measurements associated with each phase have not yet been reported. Another difficulty in strain determination may be caused by the chemical composition of the alloy, which could result in weak intensities for the γ' superstructure reflections, especially when using X-ray beams. This is the case for the N18 superalloy investigated in this study. Only two reflections related to the γ' phase are visible in diffraction patterns measured with a 8 keV beam in the laboratory or a 84 keV beam at the synchrotron. Therefore, the separation of the γ and γ' contributions mainly relies on the deconvolution of fundamental reflections, which is not very accurate without a high-resolution setup.

In the past decade, the versatility of the Laue technique has been greatly improved in synchrotrons by Kirkpatrick–Baez (KB) mirrors (Kirkpatrick & Baez, 1948), which reshape the incident beam to submicrometre sizes, by fast sample positioning and detector acquisitions that enable strain mapping, and by the development of analysis software that can process large volumes of data (Chung & Ice, 1999; Tamura *et al.*, 2002; Micha & Robach, 2010; Alghabi *et al.*, 2014, 2016; Tamura, 2014). The technique is now commonly used at the Advanced Light Source, the Advanced Photon Source and the European Synchrotron Radiation Facility (ESRF) to probe materials properties and provides useful insights at a scale that can also be investigated by dislocation dynamics and finite element calculations (Korsunsky *et al.*, 2012). Crystal orientations and deviatoric strains are now easily obtained from polychromatic beam measurements. Geometrically necessary dislocation densities can also be estimated from crystal local orientation gradients (Barabash & Ice, 2014). However, Laue diffraction experiments provide the crystal unit cell within a scaling factor. The energy of a reflection has to be measured to determine this unknown parameter. Until a few years ago, this was done by switching from a white-beam mode to a tunable-energy monochromatic beam mode. Recently, energy measurements with energy dispersive detectors (Send *et al.*, 2009; Robach *et al.*, 2011) or with a single-crystal filter, called the 'rainbow' method in the following (Robach *et al.*, 2013), were developed to perform this task while remaining in the polychromatic mode. The main advantage is that the stability of the incoming beam is not modified. With the tunable-energy mode, the focusing of the beam on the sample surface may change during the measurements. Accuracies close to 10^{-4} were obtained on $\Delta a/a$ in Ge single- and UO_2 polycrystals (Robach *et al.*, 2013) and a full strain analysis was performed in stressed Ge microstructures (Tardif *et al.*, 2016). Measurements with a two-dimensional energy dispersive X-ray CCD detector in a strained copper single crystal have demonstrated the advantages of single-shot acquisitions for determining the components of the full strain tensor (Abboud *et al.*, 2017). The energy resolution of the pn-junction CCD is of the order of several hundred electronvolts depending on the Laue spot energy (130 eV at 5 keV) and yields strain accuracies close to 10^{-3}.

In this work, Laue microdiffraction coupled with energy measurements is used to determine full elastic strain tensors at the grain scale for the γ and γ' phases in nickel-based superalloy samples. Specific model microstructures are investigated using both an energy dispersive point detector and the rainbow technique. We compare the accuracy of the resulting crystal lattice parameters and assess the ability of the two techniques to separate strains arising from the γ and γ' phases in an alloy with a lattice mismatch close to 10^{-3} Å. Phase strain sensitivity is addressed with measurements in microstructures with 200 or 2000 nm γ' precipitate sizes.

2. Experimental details

2.1. Sample description

Cylindrical specimens were cut by electro-discharge machining in a sector of a high-pressure turbine disc of N18 nickel-based superalloy produced by powder metallurgy at Safran Aircraft Engines (see composition in Table 1). After a supersolvus solution treatment (4 h at 1478 K) followed by an aging treatment, the microstructure was characterized by a 40 µm average grain size (Fig. 1*a*) and one population of secondary γ' strengthening precipitates embedded in a γ

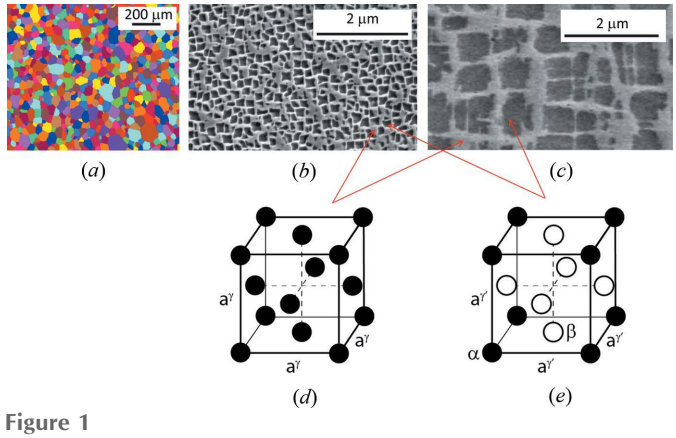

Figure 1
(*a*) Electron backscattered diffraction image obtained in a scanning electron microscope, revealing γ grains (random colors) and showing an average grain size of 40 µm with a distribution ranging from 5 to 200 µm. (*b*), (*c*) Scanning electron micrographs showing secondary γ' precipitates (dark gray) embedded into the γ matrix (light gray). (*d*), (*e*) The crystallographic structure of, respectively, the γ (A1) and the γ' ($L1_2$) phases (see text for detail).

Table 1
Chemical composition (weight %) of the investigated N18 nickel-based superalloy samples.

Ni	Co	Cr	Mo	Al	Ti	Hf	Zr	B	C
Balance	15.5	11.4	6.4	4.5	4.5	0.5	0.03	0.01	0.01

matrix phase. The γ phase is a solid solution with a random distribution of the chemical species on a face-centered cubic lattice (see Fig. 1*d*). The γ' phase exhibits an ordered face-centered cubic structure ($L1_2$) in which the corner of the cubic lattice and the face centers are non-equivalent atomic sites [α and β in Fig. 1(*e*)]. Some chemical elements occupy preferentially the α or the β sites, like aluminium and nickel, respectively. Others, like titanium, occupy indifferently the two sites. The space groups of the γ and γ' phases are, respectively, $Fm\overline{3}m$ (225) and $Pm\overline{3}m$ (221). The 200 nm γ' precipitate microstructure is obtained after an aging treatment of 1 h at 1173 K followed by an air quench. For the 2000 nm γ' precipitate microstructure, the aging treatment consists of a cooling ramp from 1478 to 1173 K with a slope of 7 K min^{-1} and a subsequent air quench (Fig. 1*c*). The lattice mismatches ($\Delta a = a_{\gamma'} - a_{\gamma}$) were determined from a Rietveld analysis of the diffraction patterns related to the two microstructures. The values are -3.5×10^{-3} Å for the sample with 200 nm precipitates and -6.7×10^{-3} Å for the sample with 2000 nm precipitates.

The two samples investigated had diameters of 6.22 mm and heights of 10 mm. The main characteristics of each microstructure are summarized in Table 2. For each sample, X-ray measurements were performed in a circular cross section which was polished by hand and then electrochemically to reduce stresses introduced by the machining operations.

2.2. Measurement conditions

Laue microdiffraction measurements were carried out on the BM32 French CRG-IF end-station of the ESRF (Ulrich *et al.*, 2011). The incoming 5–22 keV polychromatic beam was focused with KB mirrors to have a submicrometre spot size on the sample surface, which was tilted by 40° with respect to the X-ray beam (see Fig. 2). The Laue patterns arising from the sample were collected by a 2048 × 2048 pixel MAR165 circular CCD detector located about 70 mm above the sample. Fluorescence spectra were recorded using a silicon drift KETEK VITUS H7 detector mounted on a two-axis translation stage. The incoming beam flux was continuously monitored by a photodiode. An optical microscope with a focal depth less than 1 µm was used to position the sample surface in the beam spot using the sample translation stage along the $\hat{\mathbf{e}}_3^{\mathrm{S}}$ direction (defined in Fig. 2). The KB mirrors and sample stage were mounted on an antivibration table. A tilt compensation loop associated with one of the two KB mirrors ensured that the vertical displacement of the beam was less than 2 µm per 24 h while the sample or measurement devices were being displaced (*e.g.* CCD, optical microscope). The displacements caused by temperature oscillations in the hutch were also compensated by this loop (Leclere *et al.*, 2016).

Table 2
Main characteristics of the investigated N18 nickel-based superalloy samples (polycrystalline cylinders of diameter 6.22 mm and height 10 mm with a 40 µm average grain size).

Labeling	γ' precipitate size (nm)
S1	200
S2	1100–3000

A strain-free single-crystalline Ge wafer and copper lines were glued on the sample surface for experimental geometry, beam size and position calibrations (Ulrich *et al.*, 2011). The Ge crystal was also utilized to set up the energy measurements with a side energy dispersive detector (Robach *et al.*, 2011) and a diamond filter (Robach *et al.*, 2013). When this filter is used, Laue patterns have to be collected for different rotation angles θ_{f}. Calibration of the diamond orientation as a function of θ_{f} was performed (i) by collecting Laue patterns with an ImageStar CCD camera located close to the diamond (CCD1 in Fig. 2), which enables the indexing of many Ge dips, and (ii) by refining the orientation of the rotation axis to minimize the deviation of the Ge lattice parameters obtained from the different dips [for details see Robach *et al.* (2013)]. The term 'dip' is used to describe the attenuation of the intensity of a sample reflection of energy E_{hkl} during a θ_{f} scan. This is due to the diffraction of the diamond single crystal, which removes some photons with energy E_{hkl} from the incoming beam at a given θ_{f} angle.

The area probed by the incoming beam on the sample surface was 0.3 × 0.6 µm for the first measurement campaign and 0.8 × 0.8 µm for the second. With a 5–22 keV polychromatic beam and the experimental geometry described above,

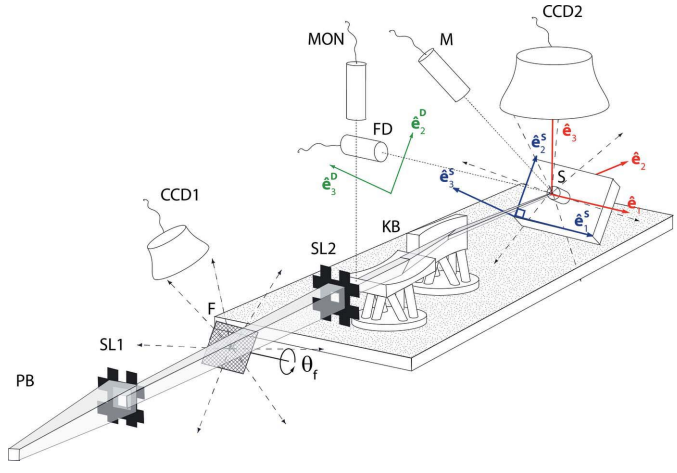

Figure 2
Schematic of the diffractometer setup with the polychromatic incident X-ray beam (PB), slits (SL*x*), diamond filter (F), KB focusing mirrors mounted on hexapods, polycrystalline sample (S), two-dimensional CCD*i* detectors ($i = 1, 2$) and energy dispersive side detector (FD). The photodiode (MON) is used for beam flux measurements and the optical microscope (M) for sample positioning. θ_{f} corresponds to the filter rotation angle. $\hat{\mathbf{e}}_i^{\mathrm{S}}$, $\hat{\mathbf{e}}_i^{\mathrm{D}}$ and $\hat{\mathbf{e}}_i$ ($i = 2, 3$) are the coordinate systems of the sample, the energy dispersive detector and the laboratory, respectively. The trajectories of the diffracted beams are symbolized by multi-directional dashed arrows (see text for more detail). Dotted lines are guidelines.

the characteristic penetration depth in the investigated samples was estimated to be in the range of 5–20 µm. As the average grain size of the sample was 40 µm, a Laue pattern consists of diffraction spots arising from the γ and γ' phases and is associated with only a few crystallites, depending on the crystal deformation and beam position with respect to the grain boundaries. With a 0.5 s exposure time, about 50 Laue spots were typically visible in the diffraction patterns (see Fig. 3*a*). In the following, these spots are divided into two categories: those corresponding to fundamental reflections, for which the three Miller indices have the same parity, and superstructure reflections with Miller indices of different parities. The fundamental reflections are related to the face-centered cubic lattice. Owing to the cube–cube orientation relationship between the γ and the γ' phases, they correspond to the sum of the intensities diffracted by the two phases and thus provide information originating from the whole irradiated volume. The superstructure reflections are related to the chemical ordering of the face-centered cubic lattice. They are thus only due to diffraction by the γ' phase.

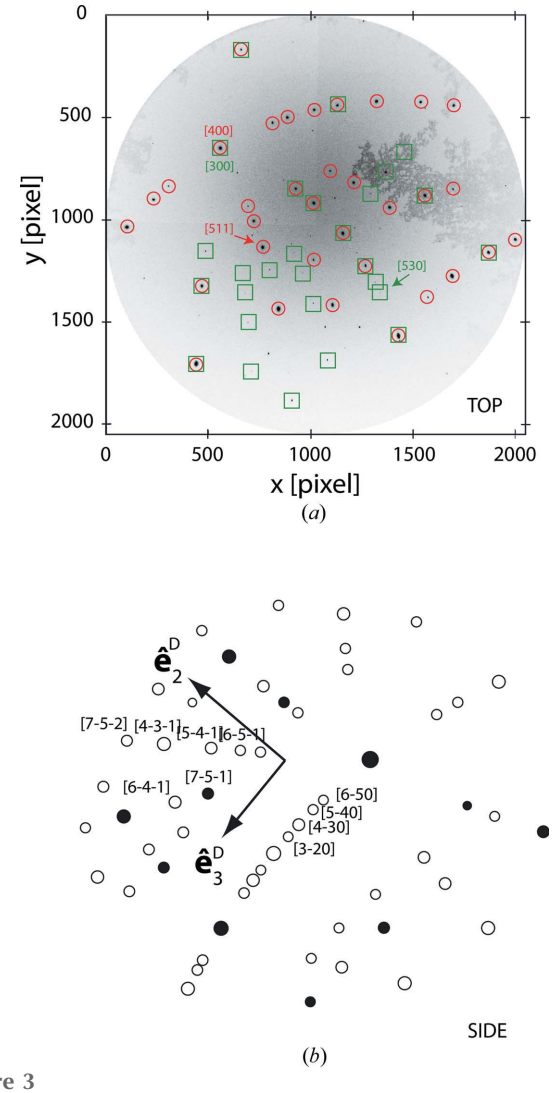

Figure 3
(*a*) Laue pattern recorded by CCD2 in sample S2. Circle and square symbols correspond, respectively, to the fundamental and superstructure reflections of the same crystallite. Arrows indicate the reflections used to analyze dip profiles in Fig. 6. (*b*) Simulated Laue pattern on the energy dispersive detector side. Closed symbols correspond to fundamental reflections and open symbols to superstructure reflections. $\hat{\mathbf{e}}_i^D$ ($i = 2, 3$) is the coordinate system related to the *yz* detector translation stage (see Fig. 2). Indexed reflections are reachable within the translation and the energy range of the detector.

In this work, geometrical calibrations and diffraction pattern analyses were performed with the *LaueTools* software developed by the BM32 beamline staff of the ESRF (Micha & Robach, 2010). This open-source Python-based code allows the analysis of single files or file series; its multiprocessing capacities greatly speed up data processing. The simulation capacities of the software were also used in energy measurements to provide the Laue pattern on the sample side when using the energy dispersive point detector or to predict the positions of dips when using the rainbow filter.

For Bragg reflection energy measurements, we followed operating procedures described in previous articles (Robach *et al.*, 2011, 2013). In short, when using the energy dispersive point detector, once the Laue pattern of the sample was indexed, it was simulated on the detector side. The detector was then translated by a motorized stage ($\hat{\mathbf{e}}_i^D$ coordinate system in Fig. 2) so that its 10 mm^2 active window intercepted a selected Bragg reflection. An energy spectrum was collected in tens of seconds for fundamental reflections (Miller indices with the same parity) and a few hundred seconds for superstructure reflections (Miller indices with different parities). An additional spectrum was also collected out of the Bragg position to clearly distinguish the peak arising from the reflection from those arising from the fluorescence of all the chemical species listed in Table 1. When the diamond filter was employed, the indexed Laue pattern of the sample and the energy calibration table that relates the rotation angle θ_f to the energies of all diamond $(hkl)_{dia}$ reflections within the 5–22 keV energy range were used to estimate, for each sample $(hkl)_s$ reflection, the θ_f angle at which a dip would be visible on the intensity profile recorded during a θ_f scan. This step is necessary for selecting the range of the θ_f scan, such that (i) the intensity attenuation is large, (ii) dips related to harmonic energies are avoided and (iii) the acquisition time of dip profiles is minimized. In the following, large and fine θ_f scans are analyzed. In large scans, several dips were recorded and the energies of several reflections were used in the data analysis, thus providing a better estimate of uncertainties. A scan of several thousand points lasted a few hours. In fine scans, only one dip profile was analyzed and less than half an hour was required for data acquisitions.

3. Theoretical background

The first step of the analysis procedure of a Laue pattern mainly consists of determining the peak positions on the CCD image after background subtraction. Then, given a crystal structure, the Miller indices of the Laue spots arising from the same crystallite are obtained by matching the experimental pattern with simulated ones. Once the pattern is indexed, scalar products between four noncollinear diffraction unit

vectors $\hat{\mathbf{u}}_{q_i}$ corresponding to the reflections of known Miller indices (h_i, k_i, l_i) are calculated. This allows the reciprocal lattice vectors $(\mathbf{b}_1, \mathbf{b}_2, \mathbf{b}_3)$ to be expressed as a function of the $\hat{\mathbf{u}}_{q_i}$ vectors (Chung & Ice, 1999):

$$\begin{bmatrix} \mathbf{b}_1 \\ \mathbf{b}_2 \\ \mathbf{b}_3 \end{bmatrix} = ||\mathbf{q}_1|| \begin{bmatrix} h_1 & k_1 & l_1 \\ h_2 & k_2 & l_2 \\ h_3 & k_3 & l_3 \end{bmatrix}^{-1} \begin{bmatrix} \mathbf{u}_{q_1} \\ c_1\mathbf{u}_{q_2} \\ c_2\mathbf{u}_{q_3} \end{bmatrix}, \tag{1}$$

where $||\mathbf{q}_1||$ is unknown, $c_i = ||\mathbf{q}_i||/||\mathbf{q}_1||$ $(i = 1, 2)$ are constants and h_i, k_i, l_i are the Miller indices of $\mathbf{q}_i$. To perform multiple four-spot analyses and thus to estimate uncertainties caused by the arbitrary choice of the four reflections, the $\hat{\mathbf{u}}_{q_i}$ vectors are expressed in a fixed Cartesian system of coordinates denoted by $\hat{\mathbf{e}}_i$ $(i = 1, 2, 3)$, which is usually related to the laboratory or the sample stage (see Fig. 2). The $||\mathbf{q}_1||$ dependence is then replaced by a $||\mathbf{b}_1||$ dependence. Equation (1) becomes

$$\begin{bmatrix} \mathbf{b}_1 \\ \mathbf{b}_2 \\ \mathbf{b}_3 \end{bmatrix} = ||\mathbf{b}_1|| \begin{bmatrix} m_{11} & m_{12} & m_{13} \\ m_{21} & m_{22} & m_{23} \\ m_{31} & m_{32} & m_{33} \end{bmatrix} \begin{bmatrix} \hat{\mathbf{e}}_1 \\ \hat{\mathbf{e}}_2 \\ \hat{\mathbf{e}}_3 \end{bmatrix}, \tag{2}$$

where $||\mathbf{b}_1||$ is unknown and $(m_{11}^2 + m_{12}^2 + m_{13}^2)^{1/2} = 1$. Equation (2) provides the expression for the orientation matrix $[UB]$ (Busing & Levy, 1967). It can be used to determine the orientation and the metrics of the reciprocal lattice. If one uses

$$\mathbf{a}_i = \frac{\mathbf{b}_j \times \mathbf{b}_k}{\mathbf{b}_1 \cdot (\mathbf{b}_2 \times \mathbf{b}_3)} \quad (i, j, k) = (1, 2, 3), \tag{3}$$

a similar equation is then obtained for the coordinates of the crystal unit-cell vectors $(\mathbf{a}_1, \mathbf{a}_2, \mathbf{a}_3)$ in the fixed Cartesian system of coordinates $\hat{\mathbf{e}}_i$:

$$\begin{bmatrix} \mathbf{a}_1 \\ \mathbf{a}_2 \\ \mathbf{a}_3 \end{bmatrix} = ||\mathbf{a}_1|| \begin{bmatrix} n_{11} & n_{12} & n_{13} \\ n_{21} & n_{22} & n_{23} \\ n_{31} & n_{32} & n_{33} \end{bmatrix} \begin{bmatrix} \hat{\mathbf{e}}_1 \\ \hat{\mathbf{e}}_2 \\ \hat{\mathbf{e}}_3 \end{bmatrix}, \tag{4}$$

where $||\mathbf{a}_1||$ is unknown and $(n_{11}^2 + n_{12}^2 + n_{13}^2)^{1/2} = 1$. The coefficients g_{ij} of the metric tensor $\mathbf{g}$ and the six crystal unit-cell parameters are then given by

$$g_{ij} = \mathbf{a}_i \cdot \mathbf{a}_j, \tag{5}$$

$$||\mathbf{a}_i|| = g_{ii}^{1/2}, \quad \alpha_i = \cos^{-1}\left(\frac{g_{jk}}{g_{jj}^{1/2} g_{kk}^{1/2}}\right), \tag{6}$$

where α_i corresponds to the angle between the vectors $\mathbf{a}_j$ and $\mathbf{a}_k$. Equations (4) and (6) show that (i) the angles α_i are exactly determined and (ii) only the relative magnitude of the lattice parameters $||\mathbf{a}_1||$, $||\mathbf{a}_2||$ and $||\mathbf{a}_3||$ can be calculated.

From the definition of direct and reciprocal lattices, the interplanar distance $d_{\mathbf{q}}$ of the atomic plane family associated with the (hkl) Miller indices is given by the norm of the $\mathbf{q}$ vector. The coordinates of this vector in the reciprocal basis $(\mathbf{b}_1, \mathbf{b}_2, \mathbf{b}_3)$ are (h, k, l); they can be obtained from Bragg's law. As a consequence, one has

$$\left(\sum_{i,j=1}^{3} h_i h_j g_{ij}^*\right)^{-1/2} = \frac{m\lambda_{\mathbf{q}}}{2\sin\theta_{\mathbf{q}}}, \tag{7}$$

where $\{h_i\}$ $(i = 1, 2, 3)$ are the components of the diffraction vector $\mathbf{q}_i$. g_{ij}^* are the coefficients of the reciprocal space metric tensor. $\theta_{\mathbf{q}}$ is the angle between the incident beam and the scattering planes. m is an integer corresponding to the order of reflections and λ is the wavelength of the diffracted beam. Equation (7) leads to

$$||\mathbf{b}_1|| = \left[\frac{hc}{E_{\mathbf{q}}}\frac{m}{2\sin\theta_{\mathbf{q}}} \sum_{i,j=1,3} h_i h_j \tilde{g}_{ij}^*\right)^{1/2}\Bigg]^{-1}, \tag{8}$$

where h is the Planck constant, c is the speed of light and $E_{\mathbf{q}}$ is the energy of the hkl reflection. The values of the coefficients $\tilde{g}_{ij}^* = \mathbf{b}_i \cdot \mathbf{b}_j/||\mathbf{b}_1||^2$ are drawn from equation (2). Once $||\mathbf{b}_1||$ is known, the metrics of the crystal lattice are calculated from equations (2), (3) and (5). This shows that, in principle, four reflections of the same phase are required to determine five of the six unit-cell parameters and that the energy measurement of one reflection provides the missing lattice parameter.

In the following, the strain tensor is calculated within a general framework valid for both small and large transformations, from the metric tensors $\mathbf{g}$ and $\mathbf{g}^0$ of the strained and unstrained unit cells (Ortner, 1983; Morançais *et al.*, 2015). For a reference structure with cubic symmetry, the coefficients of the Green strain tensor $\boldsymbol{E}$ are given by

$$E_{ij} = \tfrac{1}{2}(g_{ij}/a_0^2 - \delta_{ij}), \tag{9}$$

where a_0 is the lattice parameter of the reference crystal unit cell and δ_{ij} is the Kronecker delta.

4. Choice of the a_0 lattice parameter

The unstrained lattice parameters of the γ and γ' phases were measured after chemical etching in an N18 alloy characterized by an average grain size of 10 µm and three populations of γ' precipitates of average sizes 4.3 (18), 0.21 (8) and 0.02 (1) µm (Wlodek *et al.*, 1992). They are often called primary, secondary and tertiary γ' precipitates. Although the investigated microstructures are slightly different, we may assume that the formation temperatures of the γ' precipitates are comparable. Therefore, in strain calculations, we use the values reported by Wlodek *et al.* (1992) for the secondary γ' precipitates and the γ matrix for unstrained lattice parameters ($a_0^{\gamma_{II}} = 3.5873$ Å, $a_0^{\gamma} = 3.5980$ Å) and the weighted volume fraction sum for the average alloy ($a_0^{\gamma+\gamma'} = 3.5921$ Å).

5. Results and discussion

5.1. Full elastic strain determination with the energy dispersive detector and the rainbow technique

We now analyze the measurements performed at a fixed position in sample S2 (see Table 1) with the energy dispersive point detector and the single-crystal filter.

The Laue pattern of Fig. 3(*a*) was collected in a grain close to the sample center and indexed with a simple cubic (s.c.) and a face-centered cubic (f.c.c.) unit-cell symmetry to account for the orientations of the γ' and γ phases. Fundamental and superstructure reflections are, respectively, marked with circle

and square symbols. We observe that, for about ten reflections, a fundamental and a superstructure reflection are superimposed (*e.g.* on [400] and [300] crystallographic directions). For the f.c.c. unit cell, the orientation matrix $[m]_{\rm fcc}$ in equation (2) was obtained from 21 fundamental reflections and has the following expression:

$$[m]_{\rm fcc} = \begin{bmatrix} -0.80847 & 0.11866 & 0.57611 \\ 0.27953 & -0.78496 & 0.55407 \\ 0.51817 & 0.60980 & 0.60187 \end{bmatrix}_{(\mathbf{e}_1,\mathbf{e}_2,\mathbf{e}_3)}. \quad (10)$$

For the s.c. unit cell, the orientation matrix determined from the fundamental and the superstructure reflections (82 reflections) has the following expression:

$$[m]_{\rm sc}^{\rm fund.+super.} = \begin{bmatrix} -0.80847 & 0.11873 & 0.57610 \\ 0.27954 & -0.78483 & 0.55422 \\ 0.51817 & 0.60972 & 0.60182 \end{bmatrix}_{(\mathbf{e}_1,\mathbf{e}_2,\mathbf{e}_3)}. \quad (11)$$

As explained in §2.2, the fundamental reflections are shared by the γ and the γ' phases; the orientation matrix related to the γ' phase can be obtained only if the superstructure reflections which are not superimposed on fundamental reflections are taken into account. With 52 reflections, $[m]_{\rm sc}$ has the following expression:

$$[m]_{\rm sc}^{\rm super.} = \begin{bmatrix} -0.80847 & 0.11868 & 0.57613 \\ 0.27954 & -0.78480 & 0.55424 \\ 0.51817 & 0.60984 & 0.60174 \end{bmatrix}_{(\mathbf{e}_1,\mathbf{e}_2,\mathbf{e}_3)}. \quad (12)$$

The difference between the coefficients m_{ij} in equations (11) and (12) is less than 1×10^{-4}. The effect of fundamental reflections is equivalent to a rotation of the crystal lattice by an angle of 0.14 mrad. This value is close to the accuracy provided by the experimental setup and the analysis software. The differences between equations (10) and (11) are equivalent to a disorientation angle of 0.10 mrad, showing the cube–cube orientation relationship between the γ and the γ' phases.

The pattern in the direction of the energy dispersive detector was then simulated with the *LaueTools* software. Fig. 3(*b*) shows the fundamental (filled symbols) and superstructure (open symbols) reflections as well as the detector coordinate system $\hat{\mathbf{e}}_i^{\rm D}$ ($i = 2, 3$). The labeled reflections are the ones reached within the translation and energy ranges of the detector. A fluorescence spectrum along the $[7\bar{5}\bar{1}]$ direction and one about 2° off the diffraction direction are represented in Fig. 4. The Bragg peak corresponds to the peak located close to channel 1900 and the others to the fluorescence emissions of the sample's chemical elements. Ti, Cr, Co, Ni, Mo and Bragg peaks were modeled using a least-squares fitting procedure. Gaussian profiles were assumed upon calculating the energy-channel relationship and determining the energy of the Bragg reflection (Fig. 5*a*). In principle, the calibration is realized by assuming a quadratic relationship between the fluorescence energies and channel positions in order to account for nonlinear effects of the detector at high counting rates. However, in practice, the counting rate is controlled with beam attenuators to maintain a linear behavior. Owing to the cube–cube orientation relationship between the crystal unit cells related to the γ and the γ' phases, the Bragg angles of their fundamental reflections are identical. The difference between their lattice parameters is thus only quantifiable through the energy difference of their reflections. In Fig. 5(*a*), only one peak is visible, at $E_{7\bar{5}\bar{1}}$ = 18 936 eV, indicating that the energy resolution of the detector (∼150 eV) is too large to provide phase sensitivity. The uncertainty on peak positions usually leads to errors larger than 5 eV on reflection energies and the accuracy of the calculated lattice parameters is close to 1×10^{-3} Å. A multiple peak analysis as presented by Robach *et al.* (2011) is not feasible here for fundamental reflections since only one reflection is in the translation range of the detector.

The energy, the Bragg angle and the Miller indices of the reflection were then used to determine the lattice parameter $||\mathbf{b}_1||$ in equation (8). The coordinates of the reciprocal lattice

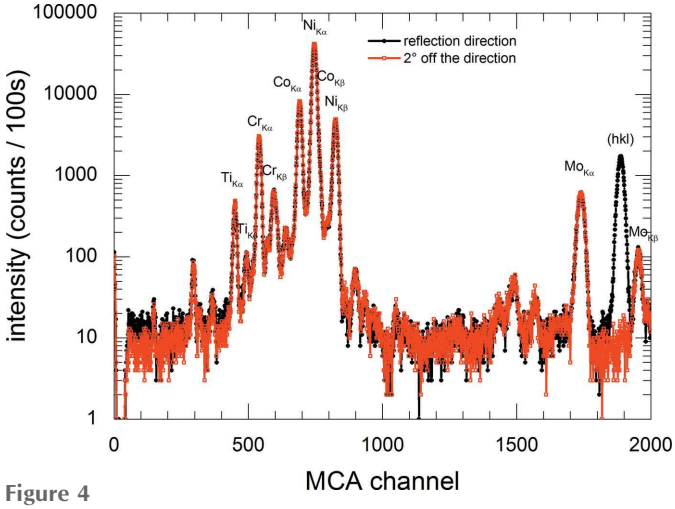

Figure 4
Energy spectra collected with the energy dispersive point detector along the $7\bar{5}\bar{1}$ reflection direction (black circles) and about 2° off the reflection direction (red squares). The most intense peaks are labeled with their corresponding chemical element and X-ray emission line.

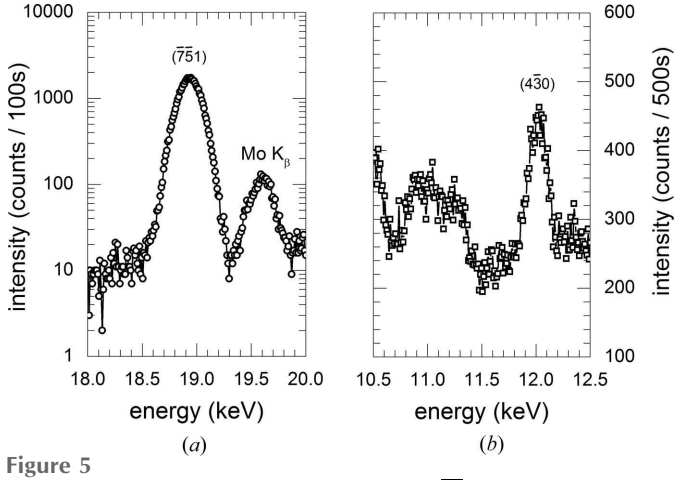

(*a*) (*b*)

Figure 5
Fluorescence spectrum associated with (*a*) the $7\bar{5}\bar{1}$ fundamental reflection and (*b*) the $4\bar{3}0$ superstructure reflection.

Table 3
Characteristics of the fundamental and superstructure reflections investigated with the energy dispersive detector (Fluo.) and the rainbow technique (Filter).

The crystal unit-cell parameters $\{\mathbf{a}_i, \alpha_i\}$ deduced using the data processing described in §3 are also given. The corresponding uncertainties (in parentheses) are related to the error associated with the energy of the reflection.

hkl	2θ (°)	Energy (eV)	FWHM (eV)	Phase	Crystal symmetry	$\|\|\mathbf{a}_1\|\|$ (Å)	$\|\|\mathbf{a}_2\|\|$ (Å)	$\|\|\mathbf{a}_3\|\|$ (Å)	α_1 (°)	α_2 (°)	α_3 (°)	$V^{1/3}$ (Å)
Fluo.												
$7\bar{5}1$	104.091	18937 (5)	206 (1)	$\gamma+\gamma'$	f.c.c.	3.5963 (9)	3.5933 (9)	3.5909 (9)	89.980 (0)	90.010 (0)	90.004 (0)	3.5935 (9)
$4\bar{3}0$	91.765	12020 (5)	163 (8)	γ'	s.c.	3.5928 (15)	3.5899 (15)	3.5877 (15)	89.992 (0)	90.001 (0)	90.004 (0)	3.5901 (15)
Filter												
511	80.162	13904 (2)	21 (3)	γ	f.c.c.	3.5986 (5)	3.5956 (5)	3.5932 (5)	89.980 (0)	90.010 (0)	90.004 (0)	3.5958 (5)
511	80.162	13932 (2)	21 (3)	γ'	s.c.	3.5914 (6)	3.5885 (6)	3.5863 (6)	89.980 (0)	90.010 (0)	90.004 (0)	3.5887 (6)
530	78.362	15931 (2)	2 (2)	γ'	s.c.	3.5936 (5)	3.5906 (5)	3.5885 (5)	89.992 (0)	90.001 (0)	90.004 (0)	3.5909 (5)

vector were calculated using equation (7) combined with the $[m]$ matrix [equation (10)]. Then the six crystal unit-cell parameters $\{\mathbf{a}_i, \alpha_i\}$ with $i = 1, 2, 3$ were determined from equations (5) and (6). Table 3 summarizes the results obtained from the Laue pattern of Fig. 3(*a*) and the energy measurements of the $7\bar{5}1$ and $4\bar{3}0$ reflections. Finally, the full elastic strain tensors related to the average alloy and the γ' phase are given in units of 10^{-3} in the crystal coordinate system by

$$E^{\gamma+\gamma'} = \begin{bmatrix} 1.1\,(0) & 0.0\,(0) & -0.1\,(0) \\ 0.0\,(0) & 0.4\,(0) & 0.2\,(0) \\ -0.1\,(0) & 0.3\,(0) & -0.3\,(0) \end{bmatrix}_{(\mathbf{a}_1,\mathbf{a}_2,\mathbf{a}_3)}, \qquad (13)$$

$$E^{\gamma'} = \begin{bmatrix} 2.0\,(2) & -0.1\,(0) & -0.1\,(0) \\ -0.1\,(0) & 1.2\,(2) & -0.1\,(0) \\ -0.1\,(0) & -0.1\,(0) & 0.6\,(2) \end{bmatrix}_{(\mathbf{a}_1,\mathbf{a}_2,\mathbf{a}_3)}, \qquad (14)$$

where the numbers in parentheses correspond to the uncertainties associated with the energy value of the two reflections.

With the 'rainbow' technique, the Laue pattern of Fig. 3(*a*) was collected for all crystal rotation angles θ_f. The integrated intensity around the maximum of each indexed reflection was then calculated as a function of the filter angle. Fig. 6 represents intensity profiles associated with the 511 fundamental reflection (Fig. 6*a*) and the 530 superstructure reflection (Fig. 6*b*). For this purpose, the θ_f angles were converted into energies using the calibration table determined from measurements in the Ge crystal. The positions of the two reflections in the Laue pattern are indicated by arrows in Fig. 3(*a*). The γ and γ' reflections are clearly visible in Fig. 6(*a*). The local minima of the double-well profile are separated by 27 eV and the peak widths are close to 20 eV. The peak width is surprisingly sharper for the superstructure reflection (1 eV). In both cases, a scan step of 0.005° and a 0.05 mm vertical gap of slits SL2 (Fig. 2) were necessary to observe dips arising from diamond diffraction. The crystal parameters derived from the 511 and 530 intensity profiles are given in Table 3. The lattice mismatch between the two phases is $\Delta a = -7.5 \times 10^{-3}$ Å. Parameters related to the γ' phase can be obtained from the two intensity profiles. We observe that they differ by 2.2×10^{-3} Å ($|\Delta a|/a = 6 \times 10^{-4}$). To better evaluate uncertainties, the previous analysis is performed on 10 intensity profiles associated with different *hkl* reflections. The values corresponding to $\|\mathbf{a}_i\|$ are represented by closed symbols in Fig. 7 as a function of the probed phase. For each lattice parameter set, horizontal solid lines correspond to the average values and error bars to the standard deviation. Despite the 1–2 eV accuracy of reflection energies leading to 2–4 $\times 10^{-4}$ Å uncertainties, the calculated lattice parameters are spread out

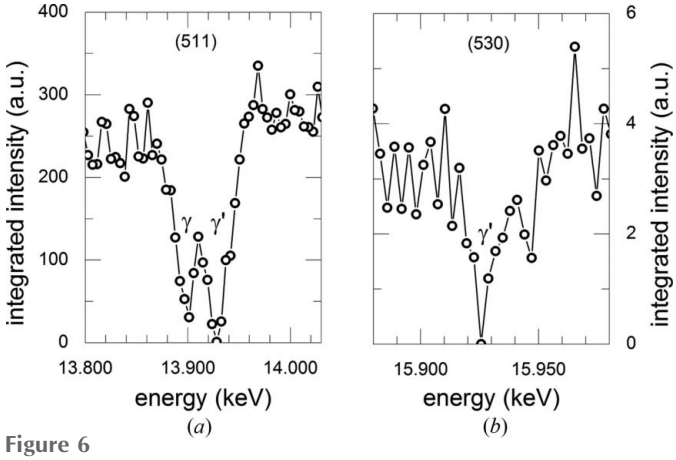

Figure 6
Laue spot energy associated with (*a*) the 511 fundamental reflection and (*b*) the 530 superstructure reflection from measurements performed with the diamond filter.

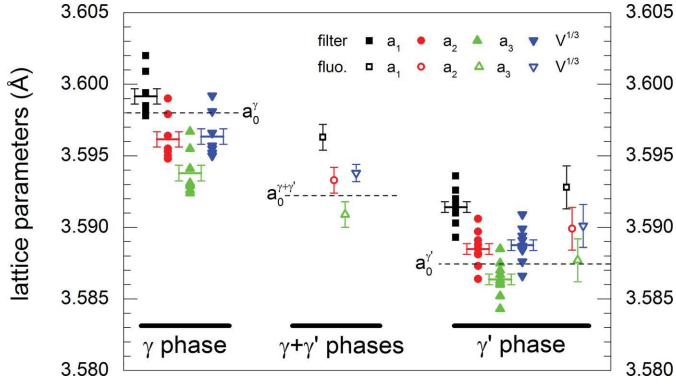

Figure 7
Norm of the crystal unit-cell axes determined using the energy dispersive detector and the rainbow filter techniques at a fixed sample position.

over 5×10^{-3} Å. The standard deviation is 5×10^{-4} Å for the γ phase and 4×10^{-4} Å for the γ' phase. When the same analysis was performed on the Laue patterns collected in the Ge single crystal, the lattice parameter spread was close to 3×10^{-3} Å. This suggests that the variation in lattice parameter values in the alloy is mainly related to instrumental corrections rather than to energy shifts of diffracted spots caused by the long-range elastic fields arising from the lattice coherency between the γ and γ' phases. Fig. 7 shows that a multiple reflection analysis is necessary to determine lattice parameters with an uncertainty of $\pm 2.5 \times 10^{-3}$ Å. The results obtained from energy measurements with the energy dispersive detector are also represented in Fig. 7 (open symbols). For the γ' phase, all uncertainties considered, the obtained values are similar to those obtained with the rainbow technique.

The results shown in Fig. 7 also tend to indicate that the crystal unit cell has an orthorhombic symmetry. This must be interpreted with caution owing to the accuracy of the measured lattice parameters. For the unstrained Ge crystal used to calibrate the rainbow method, the deviation from the expected cubic symmetry $|(a_i - a_1)/a_1 - 1|$ $(i = 2, 3)$ was close to 5×10^{-4}. This is equivalent to errors of up to 3×10^{-3} Å on lattice parameter values. In Fig. 7, $|a_2 - a_1| = 2 \times 10^{-3}$ Å and $|a_3 - a_2| = 3 \times 10^{-3}$ Å. It is therefore not possible to conclude that the crystal unit cell is non-cubic.

The average lattice parameters determined with the rainbow technique are listed in Table 4. Assuming cubic symmetry for the crystal unit cell, the strain of the γ and γ' phases are, respectively, -3×10^{-4} and 5×10^{-4} with an uncertainty of $\pm 7 \times 10^{-4}$. The 7.5×10^{-3} Å lattice mismatch leads to a negative constrained misfit parameter $\delta'_c = 2(a^{\gamma'} - a^{\gamma})/(a^{\gamma'} + a^{\gamma})$ of -2×10^{-3}. Using the values listed in Table 4 and equation (9), the full elastic strain tensor components in the crystal coordinate system are given for the γ and γ' phases in 10^{-3} units by

$$E^{\gamma'}_{sc} = \begin{bmatrix} 1.1\,(7) & 0.1\,(2) & -0.1\,(2) \\ 0.1\,(2) & 0.3\,(7) & 0.1\,(2) \\ -0.1\,(2) & 0.1\,(2) & -0.3\,(7) \end{bmatrix}_{(\mathbf{a}_1, \mathbf{a}_2, \mathbf{a}_3)}, \quad (15)$$

$$E^{\gamma}_{fcc} = \begin{bmatrix} 0.3\,(7) & -0.1\,(2) & -0.1\,(2) \\ -0.1\,(2) & -0.5\,(7) & 0.2\,(2) \\ -0.1\,(2) & 0.2\,(2) & -1.2\,(7) \end{bmatrix}_{(\mathbf{a}_1, \mathbf{a}_2, \mathbf{a}_3)}. \quad (16)$$

After measuring reflection energies with the energy dispersive point detector and the diamond single-crystal filter in a multicomponent alloy with a lattice mismatch close to 10^{-3} Å, we can make the following remarks:

(*a*) With the energy dispersive point detector, the presence of several chemical elements in the alloy enables accurate determinations of the energy-channel relationship from the spectrum with the Bragg peak. Good accuracy is obtained when the calibration is performed on each collected spectrum. The uncertainties on the lattice parameters of the N18 superalloy are close to $\pm 2 \times 10^{-3}$ Å ($|\Delta a|/a = 6 \times 10^{-4}$). The 150 eV resolution of the detector is too large to accurately determine the lattice parameters of the γ phase. Therefore, measurements provide these quantities for the average alloy and the γ' phase. Owing to the limited translation range of the detector, shadowing caused by the sample stage and crystal symmetry, the energies of fundamental and superstructure reflections are not always measurable at every sample position. To be used in an automatic mode, energy measurements of different Laue spots would require maps with a counting time larger than 100 s per point, that is, acquisition times longer than ten hours.

Table 4
Phase dependence of the lattice parameters (in angströms) measured with the rainbow technique at a fixed sample position.

a_0 is the unstrained lattice parameter measured by Wlodek *et al.* (1992).

Phase	$\|\|\mathbf{a}_1\|\|$	$\|\|\mathbf{a}_2\|\|$	$\|\|\mathbf{a}_3\|\|$	$V^{1/3}$	a_0
γ	3.5991 (25)	3.5961 (25)	3.5938 (25)	3.5963 (25)	3.5980
γ'	3.5914 (25)	3.5885 (25)	3.5864 (25)	3.5888 (25)	3.5873

(*b*) With the diamond single-crystal filter (the rainbow method), energy calibration is performed only once from several Laue patterns collected from a Ge single crystal. The accuracy of the measured energies is close to 2 eV, which is equivalent to uncertainties of about 5×10^{-4} Å on the lattice parameter values. This makes it possible to determine these quantities for the γ and γ' phases separately. Hundreds of Laue patterns collected in less than half an hour usually provide several intensity dips, which makes multiple peak analysis possible and thus grants better confidence in the results. The uncertainties on the lattice parameter values are close to $\pm 2.5 \times 10^{-3}$ Å. This value may be reduced by an analysis of the diffraction data for constant penetration depths of the X-ray beams into the material. The method is applicable to every sample position and can be used in an automatic mode with acquisitions of about 15 min per sample position.

(*c*) The crystal lattice parameters determined with the two methods at a fixed sample position are similar. The uncertainties are of the same order of magnitude, 2.5×10^{-3} Å, which leads to uncertainties close to 1×10^{-3} on the diagonal components of the strain tensor. However, better phase sensitivity is obtained with the rainbow method.

5.2. Effect of precipitate size

In the following, we investigate the effect of the secondary γ' precipitate size on the lattice parameters and the residual elastic strain in the microstructures labeled S1 and S2 in Table 2. As in the previous section, results from energy measurements with the point detector and rainbow filter are compared.

For the sake of clarity, Fig. 8(*a*) represents the lattice parameter in the cubic approximation ($\overline{a} = V^{1/3}$) determined using the energy dispersive detector in six grains: three with 200 nm γ' precipitates and three with γ' precipitates that have an average size of 2000 nm (see Fig. 1). Dashed lines correspond to the unstrained lattice parameters of each phase (Wlodek *et al.*, 1992) and of the average alloy. The six

parameters of the crystal unit cell are provided in Appendix *A*. As previously explained, multiple peak analysis is not possible and the energy of a fundamental and a superstructure reflection are not always measurable for a given grain orientation. This is the case for the grains investigated in the S1 microstructure [open squares in Fig. 8(*a*)]. For each grain, the lattice parameter of either the average alloy or the γ' phase was determined. The lattice parameter of the γ' phase (P3 in grain 3) is very close to the lattice parameter of the average alloy (A1 and A2). By considering the uncertainties, we may assume that the lattice mismatch is less than 3×10^{-3} Å. For microstructure S2, measurements yield a difference between the lattice parameters of the average alloy and of the γ' phase of 1.8×10^{-3} Å in grain 1 and 3.7×10^{-3} Å in grain 3 [open circles in Fig. 8(*a*)]. Since the volume fraction of the γ' phase is close to 50%, the lattice mismatch is qualitatively twice this value according to Vegard's law for the concentration dependence of the lattice parameters.

A more precise analysis can be done if we consider the results obtained with the diamond filter. Fig. 9 represents the dip profiles of a fundamental reflection measured in grains in samples S1 and S2. For the larger precipitate size (Fig. 9*a*), the γ and γ' contributions are clearly visible; with multiple dip analyses, we obtain a lattice mismatch of -8.5×10^{-3} Å. This value is close to the value -7.6×10^{-3} Å associated with the results of Fig. 7, which corresponds to a different grain of the same microstructure. For the smaller precipitate size (Fig. 9*b*), the contributions of the γ and γ' phases cannot be separated from the dip profile. We may reasonably assume that the energy difference is less than 10 eV, which corresponds to a lattice mismatch of -2×10^{-3} Å. Fig. 8(*b*) summarizes the results obtained with multiple peak analyses from measurements with the crystal filter in the same grains as in Fig. 8(*a*). Even if a single grain was investigated for the smaller precipitate size, the trends qualitatively inferred from energy measurements with the point detector are confirmed with better confidence: a lattice mismatch Δa close to -8×10^{-3} Å for the 2000 nm precipitates and close to -2×10^{-3} Å for the 200 nm precipitates. We observe that, for the largest size, the lattice parameter of the γ phase is close to its undeformed value (dashed line), in contrast to the parameter of the γ' phase, which is still constrained by the microstructure. The constrained misfit parameters δ'_c associated with the two precipitate sizes are close to -5×10^{-4} and -24×10^{-4}.

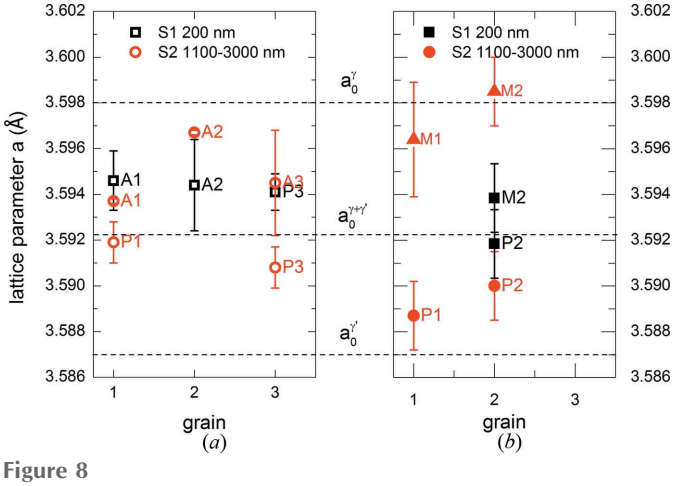

Figure 8
Cubic lattice parameters determined in different grains of microstructures S1 and S2 with (*a*) the energy dispersive point detector and (*b*) the rainbow filter. The labels A, P and M indicate whether data points correspond to the average alloy, the γ' precipitates or the γ matrix, respectively. Dashed lines are related to the unstrained lattice parameters of the γ and γ' phases and the average alloy.

The measurements reported in Fig. 8(*b*) allow us to determine the residual elastic strain tensors related to each phase. We obtain the following expressions for grain 2 related to the microstructure with an average precipitate size of 200 nm:

$$E^{\gamma'}_{sc} = \begin{bmatrix} 1.2\,(8) & -0.1\,(2) & 0.3\,(2) \\ -0.1\,(2) & 1.2\,(8) & -0.1\,(2) \\ 0.3\,(2) & -0.1\,(2) & 1.2\,(8) \end{bmatrix}_{(\mathbf{a}_1,\mathbf{a}_2,\mathbf{a}_3),\ 200\ \text{nm}}, \quad (17)$$

$$E^{\gamma}_{fcc} = \begin{bmatrix} 1.2\,(8) & -0.1\,(2) & 0.3\,(2) \\ -0.1\,(2) & -1.2\,(8) & -0.1\,(2) \\ 0.3\,(2) & -0.1\,(2) & -1.2\,(8) \end{bmatrix}_{(\mathbf{a}_1,\mathbf{a}_2,\mathbf{a}_3),\ 200\ \text{nm}}. \quad (18)$$

For grain 2 related to the microstructure with 2000 nm precipitates, we have

$$E^{\gamma'}_{sc} = \begin{bmatrix} 0.8\,(7) & 0.1\,(2) & -0.1\,(2) \\ 0.1\,(2) & 0.8\,(7) & -0.1\,(2) \\ -0.1\,(2) & -0.1\,(2) & 0.8(7) \end{bmatrix}_{(\mathbf{a}_1,\mathbf{a}_2,\mathbf{a}_3),\ 2000\ \text{nm}}, \quad (19)$$

$$E^{\gamma}_{fcc} = \begin{bmatrix} 0.1\,(7) & 0.1\,(2) & -0.1\,(2) \\ 0.1\,(2) & 0.1\,(7) & -0.1\,(2) \\ -0.1\,(2) & -0.1\,(2) & 0.1\,(7) \end{bmatrix}_{(\mathbf{a}_1,\mathbf{a}_2,\mathbf{a}_3),\ 2000\ \text{nm}}. \quad (20)$$

These results show that when the lattice mismatch is less than 2×10^{-3} (200 nm precipitates) the elastic dilatational strain is close to 1.2×10^{-3} in absolute value (negative for the γ phase and positive for the γ' phase). For a lattice mismatch close to 8×10^{-3} (2000 nm precipitates), the strains are close to zero for each phase.

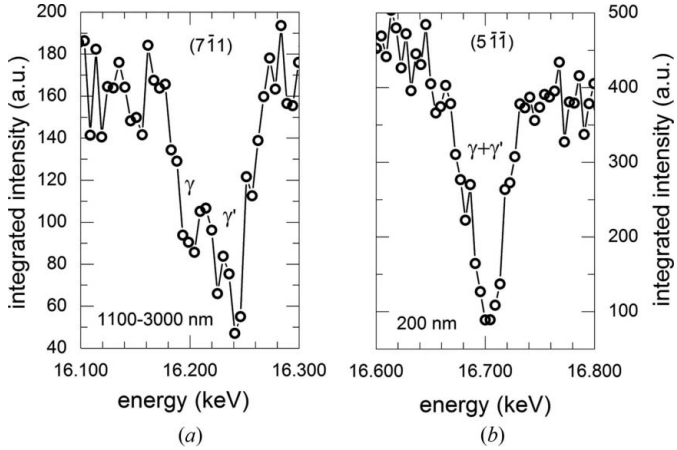

Figure 9
Influence of the γ' precipitate size on a dip profile measured with the filter technique. The average size is 2000 nm in (*a*) and 200 nm in (*b*).

Table 5
Characteristics of the fundamental and superstructure reflections investigated with the energy dispersive point detector.

The crystal unit-cell parameters $\{\mathbf{a}_i, \alpha_i\}$ drawn from the data processing described in §3 are also given.

Size (nm)	Grain	Phase	Reflection (*hkl*)	2θ (°)	Energy (eV)	$\|\|\mathbf{a}_1\|\|$ (Å)	$\|\|\mathbf{a}_2\|\|$ (Å)	$\|\|\mathbf{a}_3\|\|$ (Å)	α_1 (°)	α_2 (°)	α_3 (°)	$V^{1/3}$ (Å)
2000	1	$\gamma+\gamma'$	$7\bar{5}\bar{1}$	104.09	18936 (0)	3.5965	3.5936	3.5912	89.980	90.010	90.004	3.5937 (1)
2000	2	$\gamma+\gamma'$	$3\bar{7}1$	100.95	17164 (0)	3.5968	3.5968	3.5967	89.997	90.130	89.999	3.5967 (1)
2000	3	$\gamma+\gamma'$	517	104.600	18880 (12)	3.5961 (23)	3.5943 (23)	3.5930 (23)	89.995	90.005	89.995	3.5945 (23)
2000	3	γ'	416	104.600	16356 (4)	3.5924 (8)	3.5906 (8)	3.5893 (8)	89.995	90.005	89.995	3.5908 (9)
2000	1	γ'	$4\bar{3}0$	91.7650	12014 (3)	3.5946 (9)	3.5917 (9)	3.5895 (9)	89.992	90.001	90.004	3.5919 (9)
200	1	$\gamma+\gamma'$	$\bar{1}7\bar{3}$	103.501	16869 (6)	3.5962 (13)	3.5947 (13)	3.5929 (13)	89.998	89.996	89.992	3.5946 (13)
200	2	$\gamma+\gamma'$	$31\bar{5}$	99.003	13416 (4)	3.5988 (11)	3.5957 (11)	3.5930 (11)	89.980	90.020	89.997	3.5958 (10)
200	2	γ'	$31\bar{6}$	91.001	16442 (5)	3.5895 (11)	3.5864 (11)	3.5837 (11)	89.980	90.020	89.997	3.5865 (11)
200	3	γ'	$\bar{2}35$	106.930	13238 (3)	3.5981 (9)	3.5941 (9)	3.5904 (9)	89.987	90.015	90.006	3.5941 (8)

6. Residual stresses

The experimental determination of the elastic moduli related to the unstrained γ and γ' phases is a tedious task which is outside the scope of this study. To estimate the residual stresses related to the measured strains, the three elastic moduli of the single crystals, C_{11}, C_{12} and C_{44}, were determined from the Voigt and Reuss average coefficients (see details in Appendix *B*). The two methods yield differences of the order of 10 MPa in the crystal coordinate system, and an uncertainty on strains of 10×10^{-3} is equivalent to an uncertainty on stresses of 200 MPa. In nickel-based powder metallurgy superalloys used in high-pressure turbine discs, the yield strength at room temperature is of the order of 1200 MPa. The accuracy of the measured stresses is thus good enough to characterize the effect of surface treatments that introduce high residual stresses (*e.g.* shot-peening, deep rolling, sand blasting) but not sufficient to investigate coherency stresses between phases or stress redistributions during thermal and mechanical loadings. To do so, accuracies of the order of several tens of MPa must be reached. We have shown that the uncertainty on strains mainly relies on the spread of the lattice parameter value (see Fig. 7). The standard deviation being close to 5×10^{-4}, stress accuracies close to 20–30 MPa should be achievable with the rainbow method by improving data processing.

7. Conclusion

In this work, Laue microdiffraction coupled to energy measurements in the polychromatic mode was employed to determine the full elastic strain tensor components at the phase scale and at the grain scale in a nickel-based powder metallurgy superalloy. The energy determination of the Bragg reflections was assessed with the help of an energy dispersive point detector and the rainbow filter technique. Measurements were performed in coarse-grained microstructures with an average grain size of 40 µm, in which the γ' precipitates and γ matrix crystal unit cells exhibit a cube–cube orientation relationship.

From the analysis of fundamental reflections in samples with average precipitate sizes of 200 or 2000 nm, we demonstrated that the 1 eV energy resolution provided by the filter-based technique is suited for distinguishing the γ phase from the γ' phase when the lattice mismatch $|\Delta a|$ is larger than 2×10^{-3} Å. This was not feasible with the energy dispersive detector because of its 150 eV energy resolution, which results in uncertainties of up to 10 eV for the energy of *hkl* reflections. In that case, the collected data refer to the average alloy. The uncertainty related to the unknown crystal lattice parameter in the four-spot analysis was close to $\pm 2.5 \times 10^{-3}$ Å for the two methods. For the smallest precipitate size, the lattice mismatch $|\Delta a|$ was less than 2×10^{-3} Å and dilatational strains close to -1.5×10^{-3} and $+1.5 \times 10^{-3}$ were recorded, respectively, in the γ and γ' phases. For the largest precipitate size, the lattice mismatch was close to 8×10^{-3} Å and the elastic strains were lower than 1×10^{-3} for the two phases.

From a technical perspective, we also demonstrated that the translation range and acquisition time of the energy dispersive point detector lead to important limitations on the number of measurable reflections and the compatibility with automatic operation. In addition, energy measurements were not always feasible owing to the crystal orientation, its symmetry and the experimental setup. With the 'rainbow' filter, the energy of several *hkl* reflections can be determined irrespective of the crystal orientation and symmetry after a 15–30 min acquisition. This leads to better confidence in the data analysis. The technique is adapted to automatic data acquisition and therefore suitable for sample mapping.

γ–γ' coherency strains and their relationship with the mechanical response of a material have been investigated in depth using diffraction techniques based on peak profile analyses in single crystals of nickel-based superalloys. In this study, we showed that Laue microdiffraction is now able to perform a similar task, but at the grain scale in polycrystals and with mapping capacities. This provides helpful data for understanding the relationship between the alloy microstructure of grains and precipitates and its damage resistance (*e.g.* creep, fatigue).

APPENDIX *A*
Crystal parameters determined using energy dispersive point detector measurements

Table 5 summarizes the results obtained from energy measurements with the energy dispersive point detector in two

microstructures (labeled S1 and S2 in Table 2) whose average γ' precipitate size differs by one order of magnitude. Three grains are investigated for each microstructure, and fundamental and superstructure reflections are considered.

APPENDIX *B*
Calculation of the cubic crystal elastic constants from the effective isotropic elastic constants of the related polycrystal

In the Voigt (1928) and Reuss (1929) approaches, the elasticity tensor and its inverse are, respectively, averaged over all possible crystallite orientations. For cubic crystal symmetry, this leads to the following expressions for Young's modulus E, Poisson's ratio ν and the shear modulus μ of the polycrystal:

$$\begin{cases} E_{\rm V} = \dfrac{(C_{11}-C_{12}+3C_{44})(C_{11}+2C_{12})}{2C_{11}+3C_{12}+C_{14}}, \\ \nu_{\rm V} = -\dfrac{C_{11}+4C_{12}-2C_{44}}{4C_{11}+6C_{12}+2C_{44}}, \\ \mu_{\rm V} = \dfrac{C_{11}-C_{12}+3C_{44}}{5}, \end{cases} \tag{21}$$

$$\begin{cases} E_{\rm R} = \dfrac{5}{3S_{11}+2S_{12}+S_{44}}, \\ \nu_{\rm R} = -\dfrac{2S_{11}+8S_{12}-S_{44}}{6S_{11}+4S_{12}+2S_{44}}, \\ \mu_{\rm R} = \dfrac{5}{4S_{11}-4S_{12}+3S_{44}}. \end{cases}$$

The indexes V and R stand for Voigt and Reuss. $\{C_{ij}\}$ and $\{S_{ij}\}$ are, respectively, the three elastic constants and compliances (in Voigt notation) of the cubic crystal. The Zener ratio A, which quantifies elastic anisotropy, is defined as $2C_{44}/(C_{11}-C_{12})$. If we require that E, ν and A are fixed quantities, the three elastic constants can be derived from the previous sets of equations as follows:

$$\begin{cases} C_{11}^{\rm V} = E\dfrac{A+4+(A-6)\nu}{(2+3A)(1+\nu)(1-2\nu)}, \\ C_{12}^{\rm V} = E\dfrac{A-1+(4+A)\nu}{(2+3A)(1+\nu)(1-2\nu)}, \\ C_{44}^{\rm V} = EA\dfrac{5}{2}\dfrac{1}{(2+3A)(1+\nu)}, \end{cases} \tag{22}$$

$$\begin{cases} C_{11}^{\rm R} = \dfrac{E}{5A}\dfrac{3A+2-(A+4)\nu}{(1-2\nu)(1+\nu)}, \\ C_{12}^{\rm R} = \dfrac{E}{5A}\dfrac{A-1+(3A+2)\nu}{(1-2\nu)(1+\nu)}, \\ C_{44}^{\rm R} = \dfrac{E}{10}\dfrac{(2A+3)}{1+\nu}. \end{cases}$$

For $E = 216$ GPa, $\nu = 0.3$ and $A = 2.8$, C_{11}, C_{12} and C_{44} are, respectively, 233, 153 and 112 GPa with the Voigt approximation and 248, 146 and 143 GPa with the Reuss approximation. The value of A corresponds to the anisotropy ratio in the AM1 single-crystal superalloy.

Acknowledgements

The synchrotron data used in this paper were collected during ESRF experiments 32-02 778 and IN995. The authors gratefully acknowledge the BM32 staff for helpful discussions and technical support, as well as D. Locq from ONERA for the alloy development.

Funding information

This work was supported by the REMEDDIES project (ANR-13-BS09-016) of the French National Research Agency (ANR) and the French Aeronautical and Space Research Foundation (FRAE).

References

Aba-Perea, P., Pirling, T., Withers, P., Kelleher, J., Kabra, S. & Preuss, M. (2016). *Mater. Des.* **89**, 856–863.

Abboud, A., Kirchlechner, C., Keckes, J., Conka Nurdan, T., Send, S., Micha, J. S., Ulrich, O., Hartmann, R., Strüder, L. & Pietsch, U. (2017). *J. Appl. Cryst.* **50**, 901–908.

Alghabi, F., Send, S., Schipper, U., Abboud, A., Pashniak, N., Pietsch, U. & Kolb, A. (2014). *J. Instrum.* **9**, T11003.

Alghabi, F., Send, S., Schipper, U., Abboud, A., Pietsch, U. & Kolb, A. (2016). *J. Instrum.* **11**, T01001.

Barabash, R. & Ice, G. (2014). *Strain and Dislocation Gradients from Diffraction: Spatially Resolved Local Structure and Defects.* London: Imperial College Press.

Buchanan, D. J. & John, R. (2014). *Mater. Sci. Eng. A*, **615**, 70–78.

Busing, W. R. & Levy, H. A. (1967). *Acta Cryst.* **22**, 457–464.

Cao, W., Khadhraoui, M., Brenier, B., Guédou, J. Y. & Castex, L. (1994). *Mater. Sci. Technol.* **10**, 947–954.

Chung, J.-S. & Ice, G. E. (1999). *J. Appl. Phys.* **86**, 5249–5255.

Connor, L. D., Stone, H. J., Collins, D. M., Preuss, M., Hardy, M. C. & Rae, C. M. F. (2014). *Metall. Mater. Trans. A*, **45**, 2436–2444.

Dye, D., Roder, B., Tin, S., Rist, M., James, J. & Daymond, M. (2004). *Superalloys 2004*, edited by K. Green, T. Pollock, H. Harada, T. Howson, R. Reed, J. Schirra & S. Walston, pp. 315–322. Warrendale: The Minerals, Metals and Materials Society.

Hazotte, A., Bellet, D., Ganghoffer, J. F., Denis, S., Bastie, P. & Simon, A. (1992). *Philos. Mag. Lett.* **66**, 189–196.

Kirkpatrick, P. & Baez, A. V. (1948). *J. Opt. Soc. Am.* **38**, 766–774.

Korsunsky, A. M., Hofmann, F., Abbey, B., Song, X., Belnoue, J. P., Mocuta, C. & Dolbnya, I. (2012). *Int. J. Fatigue*, **42**, 1–13.

Leclere, C., Cornelius, T. W., Ren, Z., Robach, O., Micha, J.-S., Davydok, A., Ulrich, O., Richter, G. & Thomas, O. (2016). *J. Synchrotron Rad.* **23**, 1395–1400.

Micha, J.-S. & Robach, O. (2010). *LaueTools*, http://sourceforge.net/projects/lauetools/.

Morançais, A., Fèvre, M., François, M., Guel, N., Kruch, S., Kanouté, P. & Longuet, A. (2015). *J. Appl. Cryst.* **48**, 1761–1776.

Ortner, B. (1983). *Eingenspannungen*, pp. 49–68. Oberursel: Deutsche Gesellschaft fur Metallkddunde.

Preuss, M., da Fonseca, J. Q., Grant, B., Knoche, E., Moat, R. & Daymond, M. (2008). *Superalloys 2008*, pp. 405–414. Warrendale: The Minerals, Metals and Materials Society.

Reuss, A. (1929). *Z. Angew. Math. Mech.* **9**, 49–58.

Robach, O., Micha, J.-S., Ulrich, O., Geaymond, O., Sicardy, O., Härtwig, J. & Rieutord, F. (2013). *Acta Cryst.* A**69**, 164–170.

Robach, O., Micha, J.-S., Ulrich, O. & Gergaud, P. (2011). *J. Appl. Cryst.* **44**, 688–696.
Royer, A., Bastie, P. & Véron, M. (1997). *Mater. Sci. Eng. A*, **234–236**, 1110–1113.
Send, S., von Kozierowski, M., Panzner, T., Gorfman, S., Nurdan, K., Walenta, A. H., Pietsch, U., Leitenberger, W., Hartmann, R. & Strüder, L. (2009). *J. Appl. Cryst.* **42**, 1139–1146.
Stone, H., Holden, T. & Reed, R. (1999). *Acta Mater.* **47**, 4435–4448.
Stone, H., Reed, R. & Holden, T. (1999). *Scr. Mater.* **40**, 353–358.
Tamura, N. X. (2014). *Strain and Dislocation Gradients from Diffraction: Spatially Resolved Local Structure and Defects*, ch. 4, pp. 125–155. Oxford University Press.
Tamura, N., MacDowell, A. A., Celestre, R. S., Padmore, H. A., Valek, B., Bravman, J. C., Spolenak, R., Brown, W. L., Marieb, T., Fujimoto, H., Batterman, B. W. & Patel, J. R. (2002). *Appl. Phys. Lett.* **80**, 3724–3726.
Tardif, S. *et al.* (2016). *J. Appl. Cryst.* **49**, 1402–1411.
Ulrich, O., Biquard, X., Bleuet, P., Geaymond, O., Gergaud, P., Micha, J. S., Robach, O. & Rieutord, F. (2011). *Rev. Sci. Instrum.* **82**, 033908.
Voigt, W. (1928). *Lehrbuch der Kristallphysik*. Berlin, Leipzig: Teubner.
Wlodek, S., Kelly, M. & Alden, D. (1992). *Superalloys 1992*, edited by R. M. S. D. Antolovich & R. W. Stusrud, pp. 467–471. Warrendale: The Minerals, Metals and Materials Society.